Hammering sound of concrete with defects and spalling risk

Naotoshi Yasuda[a,*]

[a]*Department of Civil and Earth Resources Engineering, Kyoto University, Katsura, Nishikyo-ku, Kyoto, 615-8530, Kyoto, Japan*

Abstract

Inspection is important for preventing concrete spalling and maintaining the soundness of tunnels. Human inspection combining visual inspection and the hammering tests has a proven track record and is considered reliable. However, human inspection is time-consuming and the results vary depending on the inspector. Vibration measurement results obtained for areas with defects in unreinforced concrete sections of railway tunnels reveal that there are many defects that are overestimated the spalling risk. The objective of this study was to elucidate the causes of this overestimation. A concrete specimen with an inclined detachment was prepared, and the change in the hammering sound with the extension of the detachment was investigated. Numerical analyses were conducted to supplement the experimental results. The results reveal that the low-frequency vibrations of the defects are less likely to be transmitted by air as sound pressure. Moreover, low-frequency sounds are relatively hard to hear considering human auditory characteristics. Hence, low-frequency vibration may not affect the hammering sound. Although the presence or absence of defects can be distinguished by the hammering sound, the spalling risk cannot be accurately evaluated from the sound alone, which is one of the main reasons for spalling risk overestimation by human inspectors.

Keywords: Plain concrete, Spalling defects, Hammering test, Maintenance, Sound

*Corresponding author. Tel.:+81 75 383 7558; Fax: +81 75 383 3114
Email address: yasuda.naotoshi.3x@kyoto-u.ac.jp (Naotoshi Yasuda)

1. Introduction

Inspection is important for preventing concrete spalling and maintaining the soundness of tunnels. In Japan, a severe concrete spalling accident at Fukuoka tunnel in 1999 (Asakura and Kojima, 2003; Tsuno and Kishida, 2020) has highlighted the importance of inspection. After the accident, the inspection regime was updated and current maintenance standards for railway tunnels were established.

In the inspection process, visual inspection is first conducted. When abnormalities such as cracks and detachment are observed, a hammering test is conducted, whereby an inspector strikes a target using a steel hammer to evaluate the spalling risk through auditory and tactile sensations. Based on the test results, the robustness of the defect area against spalling is rated as α, β, or γ. When an area emits a dull sound by hammering and has spalling risk, the area is rated as α and repair or reinforcement must be promptly carried out. When an area emits a dull sound regardless of low spalling risk or has multiple cracks regardless of a clear ring, the area is rated as β and follow-up assessment is required. A hammering test is recommended once every two years, and must be carried out once every 10 or 20 years depending on the line's importance. An area where follow-up is not required, regardless of a dull sound or the multiple cracks, is rated as γ, in which case the hammering test must be carried out once every 10 or 20 years.

Human inspection combining visual inspection and the hammering test has a proven track record and is considered reliable. However, human inspection is time-consuming and the results vary depending on the inspector. Nowadays, the development of interdisciplinary technologies for tunnel inspection is accelerating to improve productivity and accuracy (Haack et al., 1995; Montero et al., 2015; Menendez et al., 2018; Fujino and Siringoringo, 2020; Huang et al., 2021). In particular, technology for automatic defect detection from photographs (Attard et al., 2018; Xue and Li, 2018; Protopapadakis et al., 2019; Jiang et al., 2019; Ren et al., 2020; Lei et al., 2021; Wang et al., 2021) and three-dimensional (3D) point cloud data (Chen et al., 2015; Zhou et al., 2021; Mizutani et al., 2022) has made remarkable progress. These approaches have been used in practical applications as an alternative or supplementary to visual inspection. Technology that can replace the hammering test is still under development. For example, an infrared method (Sakagami and Kubo, 2002; Clark et al., 2003; Maierhofer et al., 2006; Meola, 2007; Omar and Nehdi, 2017; Afshani et al., 2019; Ishikawa et al., 2021; Chun and Hayashi, 2021), mobile robotic system (Menendez et al., 2018; Loupos et al., 2018; Moreu et al., 2018; Nakamura et al., 2019), non-contact acoustic method (Mori et al., 2002; Zhu and Popovics, 2007; Oh et al., 2013; Sugimoto et al., 2019), and laser sensing method (Kurahashi et al., 2018; Yasuda et al., 2020, 2021; Wakata et al., 2022) have been proposed.

The author has previously proposed a laser sensing method and has tested it on actual tunnels. The estimated frequency of the lowest vibration mode was found to be the most useful index for the quantitative evaluation of defects (Yasuda et al., 2021). Figure 1 shows the distribution of the lowest mode frequency in the defect area rated as β in unreinforced concrete sections of tunnels. Although the frequency is concentrated around 1000 Hz, variation exists. The lowest mode frequency just before spalling was expected to be less than 100 Hz in a laboratory test when considering only its own weight (Yasuda, 2022). Based on experimental results, it is considered that there are many defects that are overestimated the spalling risk. The causes must be clarified to improve the inspection efficiency and realize hammering test mechanization. The rightmost bin is where the vibration cannot be measured in the defect area because laser-induced vibration is not sufficiently large to measure. These defects are expected to have sufficient adhesion and are rated as γ.

This study investigated the hammering sound of concrete with defects and spalling risk. Laboratory tests were performed on a concrete specimen with an inclined detachment. The change in the hammering sound with the extension of the detachment was investigated, and the causes of spalling risk overestimation by the human inspectors were elucidated.

2. Methodology

2.1. Outline of concrete specimen

The specimen had a height of 500 mm, width of 400 mm, thickness of 175 mm, and mass of approximately 80 kg, as shown in Figure 2. The inclined detachment angle was 15°. The adhesion area is defined as the attachment part on the extension line of the detachment. Assuming that the detachment along the adhesion area causes spalling, the spalling mass is approximately 30 kg. The detachment was made by embedding Styrofoam when placing the concrete and removing it after curing. The specimen preparation procedure can be found in Yasuda (2022). Anti-vibration gel (GD15-100, EXSEAL) was inserted between the specimen and the ground to suppress the wobbling caused by the unevenness at the bottom of the specimen.

The concrete mix proportions are summarized in Table 1. The maximum size of the coarse aggregate was 20 mm, and the design compressive strength was $18\,\mathrm{N/mm^2}$. The compressive and tensile strength at the age of 28 days was approximately $28\,\mathrm{N/mm^2}$ and $2.4\,\mathrm{N/mm^2}$, respectively.

2.2. Experimental procedure

The vibration and sound measurement and detachment processes were repeated alternately. The vibration and sound pressure were measured simultaneously. The detachment process simulates the crack growth caused by water leakage, temperature changes, repeated vibrations, and air pressure fluctuations induced by trains. The detachment process was modeled by gradually cutting the adhesion area from both the left and right sides using a saw (FUN-N2, Funaso). The cut length on both sides was the same at every stage.

2.3. Measurement conditions

Figure 2 shows the vibration excitation and measurement points and sound pressure measurement positions. A steel hammer (test hammer 1/4P, Hasekou) used in tunnel inspections was employed to excite vibration. The total mass was 0.22 kg, the hammerhead mass was approximately 0.11 kg (1/4 lb), and the total length was 39 cm. The shape of the tip was a cylinder, and the diameter was 17 mm. The vibration (surface velocity) was measured using a laser Doppler vibrometer (RSV-150, Polytec). The sound pressure was measured using a microphone (46AE, GRAS). The sound was measured at the distance of 50 cm in front of the specimen, with the length of the human arm as a reference. The height of the measurement positions was the same as that of the vibration measurement point. The sound pressure measurement was made at one point per hammering because only one microphone was available.

Data were obtained at the sampling frequency of 48 kHz without a filter. The distance between the vibration measurement device and the specimens was 5.0 m.

2.4. Quantification of hammering sound impression

Some differences exist between the physical properties of sound, such as the sound pressure and frequency, and subjective auditory impression.

The measured sound pressure data should be converted into psychoacoustic parameters by applying a signal processing model related to the physiological and psychological characteristics of the human hearing system. To this end, the model proposed in ISO 532-1 (ISO532-1, 2017) was used to calculate the loudness, which is the subjective perception of sound pressure. The loudness was calculated from the specific loudness pattern based on measured time-varying signals. The specific loudness was considered as an index for estimating the audibility of each frequency band, and was used to quantify the hammering sound impression in this study.

2.5. Numerical analyses

In the experimental measurement, data could only be obtained at specific positions. Hence, numerical analyses were carried out to supplement the experimental results. The analyses were conducted as linear elastic analyses in the commercial software ANSYS. Acoustic structural interaction solutions were obtained using one-way load transfer coupling analysis, wherein only the structural effect on the acoustic fluid is considered. The analysis is more computationally efficient compared with strong coupled analysis wherein both the structure and the acoustic fluid interact with each other. The specific analysis procedure is as follows: harmonic response analysis (full harmonic analysis) of the structure (concrete specimen) was carried out to determine the frequency response, and harmonic response analysis (full harmonic analysis) of the acoustic fluid (air) was carried out to determine the frequency response.

The structure was meshed using a 3D 10-node tetrahedral structural solid element (SOLID187). In the model, the shape was set to be the same as that of the specimen. The anti-vibration gel was not modeled and was instead simulated by not constraining the displacement. Hence, the structure was considered as floating concrete. The acoustic fluid was meshed using a 10-node acoustic fluid (FLUID221). The shape was modeled as a sphere with a radius of 0.8 m, and the center was the same as the center of the structure. Moreover, a second-order absorbing element (FLUID130) was attached to the exterior of the sphere to satisfy the Sommerfeld radiation condition. The objective of the analysis was to investigate the basic radiation characteristics of the sound pressure produced by defects. Therefore, the ground (the floor) was not modeled.

The material properties considered in the analyses are listed in Table 2. The concrete properties were obtained by carrying out physical property tests on the same concrete as that used in the specimen. The properties of air were those existing at the temperature of 15 °C. The damping effect for the structure was considered by using alpha (mass) damping and beta (stiffness) damping, which results in frequency-dependent damping ratios. The damping effect for the acoustic fluid was not considered because the effect is thought to be negligible.

3. Results

3.1. Hammering sound of good concrete

Before considering the hammering sound of concrete with defects, the hammering sound of good concrete was considered. Figure 3 shows the measurement results for good concrete, which were obtained by hitting a flat building wall with a thickness of 1.0 m using the steel hammer. The hammering force was the same as that used in a typical inspection. The vibration (surface velocity) was measured on a wall that was 10 cm away from the excitation point. The sound was measured at the distance of 50 cm in front of the wall, and the height was the same as that of the excitation point. The data acquisition began 0.050 s before the hammer excitation and lasted for 1.0 s. Most vibration data were noise, except those obtained immediately after the excitation. Only a small spectral peak appeared at approximately 2000 Hz owing to the multiple reflections of elastic waves between the front and back surfaces of the concrete wall. In contrast, the sound measurement result had several characteristic spectrum peaks. The vibration and sound spectra are not correlated.

Figure 4 shows the loudness of the hammering sound. The specific loudness and total loudness were calculated from the time history waveform of the sound pressure shown in Figure 3 (a). The horizontal axis in (a) represents the critical band, which describes the frequency bandwidth of the auditory filter created by the cochlea. The reference value of the corresponding frequency is also represented at the top of the figure. The vertical axis represents the magnitude of specific loudness. The loudness is measured in sone units. The total loudness is the loudness of the entire compound perceived by humans and is calculated by filtering the sum of the specific loudness at each time in the direction of time. Hence, the specific loudness is an approximate index of audibility. Details regarding the calculation can be found in ISO 532-1 (ISO532-1, 2017). The specific loudness corresponding to 1000 Hz or higher was relatively large. In particular, the specific loudness around

5000 Hz was strongly excited, and under its influence, the higher-frequency sounds were inaudible (auditory masking).

3.2. Hammering sound of concrete defects

Figure 5 shows the measurement results for the specimen before the cut. The sound was measured at position A. The response was different to that of good concrete in Figure 3, although the hammering method was approximately the same. Characteristic peaks were observed in the Fourier spectra, and the velocity and sound pressure had the same peak positions. As the frequency increased, the peak amplitudes of the sound pressure tended to be relatively larger compared with those of the velocity. Figure 6 shows the results obtained when the sounds were measured at positions B and C. The velocity spectra were selected from multiple trials such that they were approximately identical to the spectrum at position A. The sound pressure spectra were slightly different depending on the measurement position. Figure 7 shows the corresponding specific loudness. The specific loudness in the vicinity of 3000 Hz was noticeable immediately after hammering at positions A and B, and the specific loudness at position C was the smallest. The specific loudness corresponding to the range below 250 Hz was the same at all three points.

Figure 8 shows the change in the Fourier spectra of the vibration and the sound as the cut length increased. The sound was measured at position A. The frequency was displayed up to 5000 Hz because low-frequency vibration is more important than high-frequency vibration. As the cut length increased, the natural frequencies decreased. Regarding the sound pressure, as the cut length increased, the amplitude of the spectral peaks below 400 Hz decreased. Figure 9 shows the corresponding specific loudness. As the cut length increased, the specific loudness below 250 Hz decreased. At the 38 cm cut, there was almost no response below 250 Hz, regardless of the high spalling risk.

Figure 10 compares the Fourier spectra of the vibration induced by the steel hammer and impact hammer. An impact hammer with a steel tip (086C03, PCB) was used to estimate the characteristics of the steel hammer-induced vibration. The spectra of the steel hammer were the same as those shown in Figures 5 (b) and 8 (c). The spectra of the impact hammer were selected from multiple trials such that the low-frequency components matched those of the steel hammer. In both cases, the steel hammer excited higher frequency vibrations compared with the impact hammer. Figure 11 shows the corresponding force signals induced by the impact hammer. The maximum excitation force for the 0 cm and 38 cm cut was approximately 500 N and 400 N, respectively. The vibration up to 4000Hz was sufficiently excited.

Numerical analyses were carried out to supplement the experimental results. Figure 12 shows the frequency response functions in the specimen after a cut of 30 cm. The velocity measurement point was the same as that in the experiment, and the sound pressure measurement position was the same as position A. The results were calculated in the range of 100−600 Hz in 2.0 Hz increments. The alpha damping and beta damping values were 17 and 5.6×10^{-6}, respectively. The damping ratio in the range of 200−400 Hz was approximately 1 %. In the velocity spectrum, there were large responses at 210 Hz and 362 Hz, and a small response excited at 314 Hz. In the sound pressure spectrum, there were large responses at 210 Hz, 362 Hz, and 526 Hz. Figure 13 and Figure 14 show the deformation of the low-order vibration modes. These results were obtained by modal analysis. The specimen did not have a natural vibration mode around 526 Hz. In the vibration mode of 210 Hz and 362 Hz, the displacement was predominant in the x-direction. In contrast, in the vibration mode of 314 Hz, the displacement was predominant in the z-direction. This difference is responsible for the velocity and sound pressure being small around 314 Hz, as shown in Figure 12.

Figure 15 shows the spatial distribution of the maximum sound pressure in the specimen after a cut of 30 cm on the cross-section $y = -10$ (cm), where the sound measurement position A existed. The areas above the maximum value of the color bar are indicated in gray color. At 210 Hz and 362 Hz, large sound pressure was generated on the surface of the specimen and decreased according to the distance from the specimen. In contrast, at 526 Hz, large sound pressure was generated from the gap in the specimen, which modeled the detachment. The spatial distribution is complex because sound pressure was also generated from the gaps on the sides of the specimen.

Figure 16 shows the frequency response functions in the specimen after a cut of 38 cm. The results were calculated in the range of 50−250 Hz in 1.0 Hz increments. The alpha damping and beta damping values were 15 and 2.5×10^{-5}, respectively. The damping ratio in the range of 100−150 Hz was approximately 2 %. Large velocity responses were observed at 98 Hz and 152 Hz. In contrast, there was almost no sound pressure response at 98 Hz. The deformation with the natural frequencies of 98 Hz and 152 Hz was similar to that shown in Figure 13 (b) and (a), respectively. Figure 17 shows the spatial distribution of the maximum sound pressure on the cross-section $y = -10$ (cm) at 98 Hz and 152 Hz. Compared with the 30 cm cut shown in Figure 15, the magnitude of the sound pressure on the specimen was reduced. Moreover, the sound pressure decayed faster as the distance from the specimen increased.

3.3. Hammering sound before and after spalling

The hammering sound before and after spalling was investigated by blowing the specimen after a 38 cm cut was made by an impact hammer (086D05, PCB). Figure 18 shows the force signals. The hammer excitation force gradually increased until spalling occurred on the sixth impact. Immediately after the impact, the concrete block dropped by 20 mm directly below owing to its own weight, which corresponded to the gap of the detachment. The spalled concrete block was stable in that state. The seventh impact was performed by hammering the concrete block. As the excitation force increased, the excitation time became shorter and the excitation frequency increased. The maximum excitation force before spalling was approximately 5000 N. Figure 19 shows the Fourier spectra of the vibration and sound. Because of the spalling, the position of the vibration measurement of the seventh impact was higher by 20 mm compared with the other impacts. The peak vibration frequencies of the fifth impact were slightly lower than those of the third impact. This decrease was caused by the progress of the destruction of the adhesion area. By comparing the third and seventh impact, where the exciting force was approximately the same, it was found that there was little change in the peak frequencies, regardless of spalling. However, the damping rate of the vibration increased after spalling and the peak value of the spectrum decreased. Figure 20 shows the specific loudness. There was no noticeable difference between the third and fifth impact, although the vibration around 3000 Hz was damped faster in the fifth impact. Immediately after vibration excitation, the specific loudness of the seventh impact was not very different to that of other impacts. However, owing to the rapid damping of the vibration, the large excitation at a particular frequency disappeared faster compared with the other impacts.

4. Discussion

In the hammering test on good concrete, there is no correlation between the spectra of the vibration and sound, as shown in Figure 3. The hammering sound is considered to have been generated by the vibration of the hammer itself. In contrast, in the hammering test on concrete with defects, the spectra of the vibration and sound are correlated, as shown in Figure 5. The hammering sound was mainly generated by the natural vibration of the defects. The vibration sound of the hammer itself was almost inaudible in the hammering test on the concrete with defects because the sound pressure was relatively small and drowned out by that induced by the defect vibration. This can be confirmed by comparing Figures 3 (b) and 5 (b). The peak value of the spectrum with defects is more than ten times larger than that of the spectrum without defects.

As shown in Figure 8, a spectral peak of sound that is different to the natural frequency of the concrete defects was observed around 500 Hz. This was caused by the air resonance generated in the gap of the detachment, as predicted from Figures 12 and 15. Such sounds may even occur in actual gaps such as cracks and openings.

Considering that the specimen before the cut was sufficiently safe against spalling (Yasuda, 2022), it is possible to distinguish the presence or absence of defects by the hammering sound difference. The area wherein it is difficult to assess the presence or absence of a defect based on the hammering sound is considered to be sufficiently safe in terms of spalling risk.

The hammering sound was slightly different depending on the measurement position, as shown in Figure 7. The specific loudness corresponding to the range below 250 Hz was the same at all three points. The reason for this is that the wavelength of low-frequency sound waves is long compared with the difference of the measurement positions. For example, the wavelength of the 250 Hz sound wave is approximately 1.4 m, which is 14 times larger than the difference at the position of 10 cm.

As the cut length of the specimen increased, the sound pressure of the low-frequency vibration decreased, as shown in Figure 8. This result is consistent with the numerical results, as shown in Figures 12 and 16. This decrease was because the low-frequency vibrations of the defects that are lower than a certain threshold are less transmitted to the air as sound pressure. The radiation efficiency of a baffled beam, which is the ratio of the sound power radiated from a structure to that of a piston with the same size moving with the same average velocity, decreases for frequencies well below the critical frequency (Wallace, 1972a). The critical frequency is the frequency for which the wavelength of the standing wave on the beam is equal to the wavelength of the radiated acoustic wave. Similar results have been obtained for a plate (Wallace, 1972b; Berry et al., 1990). The specimen and actual defects have more complicated structure, but it is believed that the tendency is similar to that in the results obtained for these simple structures.

By comparing the results in Figures 5 (b) and 7 (a), it can be found that the specific loudness below 250 Hz was relatively small for the amplitude of the sound pressure spectrum. In contrast, the specific loudness in the vicinity of 3000 Hz was relatively large. The human auditory characteristics can also be confirmed for other cases by comparing Figures 8 and 9. The results are consistent with the equal-loudness contour characteristics defined in ISO 226. Low-frequency sounds, whose wavelength is much longer than the size of the human head, are relatively hard to hear.

Skilled inspectors employ the empirical method of checking the vibration of a defect area during hammering inspection using the palm of their hand. This is expected because the palm is most sensitive to low-frequency vibrations around 250 Hz (Reynolds et al., 1977; Griffin, 2012) and can be detected the low-frequency vibrations that are hard to hear.

As the risk of spalling increased, high-frequency sounds were relatively hard to hear, as shown in Figure 20. Because there was no clear sign of spalling, it was difficult to evaluate the spalling risk only based on the hammering sound. The hammering sound of the spalled concrete block was heard as a dull sound compared with the sound before spalling. This is attributed to the rapid damping of the vibration, which is caused by the increase of the area of contact with the surroundings. Therefore, it is considered that the hammering sound is heard as a dull sound when a particular frequency is not strongly excited or the excitation time is short.

The low-frequency vibrations of the defects are less likely to be transmitted to the air as sound pressure. Moreover, the human ear is less sensitive to such low-frequency sounds. Hence, low-frequency vibration may not affect the hammering sound. The presence or absence of defects can be distinguished by the hammering sound. However, the spalling risk cannot be accurately evaluated from the sound alone. This is one of the main reasons for spalling risk overestimation by human inspectors, as shown in Figure 1.

5. Conclusions

This study evaluated the hammering sound of a concrete specimen with an inclined detachment. The change of the hammering sound with the extension of the detachment was investigated, and numerical analyses were conducted to supplement the experimental results. The following conclusions were drawn:

(1) The presence or absence of defects can be distinguished based on the sound difference. The area wherein it is difficult to assess the presence or absence of a defect based on the hammering sound is considered to be sufficiently safe in terms of spalling risk.

(2) The low-frequency vibrations of the defects that are lower than a certain threshold are less transmitted to the air as sound pressure.

(3) Low-frequency sounds, whose wavelength is much longer than the size of the human head, are relatively hard to hear.

(4) As the risk of spalling increased, high-frequency sounds tended to be harder to hear. Nevertheless, a clear indication of spalling did not exist.

(5) The spalling risk cannot be accurately evaluated from the hammering sound alone because low-frequency vibration may not affect the sound. This is one of the main reasons for spalling risk was overestimation by human inspectors.

Human inspection combining visual inspection and the hammering test has a proven track record and is considered reliable. However, the overestimation of spalling risk is inevitable and repeated future inspections are mandated once defects are identified. Therefore, the quantification of evaluation criteria and the inspection mechanization should be realized to improve the inspection efficiency.

6. Acknowledgment

This study is a part of collaborative research with West Japan Railway Company. The supercomputer of ACCMS, Kyoto University, Japan, was used in this study.

References

Afshani, A., Kawakami, K., Konishi, S., Akagi, H., 2019. Study of infrared thermal application for detecting defects within tunnel lining. Tunnelling and Underground Space Technology 86, 186 – 197.

Asakura, T., Kojima, Y., 2003. Tunnel maintenance in japan. Tunnelling and Underground Space Technology 18, 161 – 169.

Attard, L., Debono, C.J., Valentino, G., Castro], M.D., 2018. Tunnel inspection using photogrammetric techniques and image processing: A review. ISPRS Journal of Photogrammetry and Remote Sensing 144, 180 – 188.

Berry, A., Guyader, J.L., Nicolas, J., 1990. A general formulation for the sound radiation from rectangular, baffled plates with arbitrary boundary conditions. The Journal of the Acoustical Society of America 88, 2792–2802.

Chen, H.M., Ulianov, C., Shaltout, R., 2015. 3d laser scanning technique for the inspection and monitoring of railway tunnels. Transport problems 10, 73–84.

Chun, P.j., Hayashi, S., 2021. Development of a concrete floating and delamination detection system using infrared thermography. IEEE/ASME Transactions on Mechatronics 26, 2835–2844.

Clark, M., McCann, D., Forde, M., 2003. Application of infrared thermography to the non-destructive testing of concrete and masonry bridges. NDT & E International 36, 265 – 275.

Fujino, Y., Siringoringo, D.M., 2020. Recent research and development programs for infrastructures maintenance, renovation and management in japan. Structure and Infrastructure Engineering 16, 3–25.

Griffin, M.J., 2012. Frequency-dependence of psychophysical and physiological responses to hand-transmitted vibration. Industrial health 50, 354–369.

Haack, A., Schreyer, J., Jackel, G., 1995. State-of-the-art of non-destructive testing methods for determining the state of a tunnel lining. Tunnelling and Underground Space Technology incorporating Trenchless Technology Research 4, 413–431.

Huang, M., Ninić, J., Zhang, Q., 2021. Bim, machine learning and computer vision techniques in underground construction: Current status and future perspectives. Tunnelling and Underground Space Technology 108, 103677.

Ishikawa, M., Tsukagoshi, M., Kasano, H., Nishino, H., 2021. Influence of composition and surface discoloration of concrete on active thermographic nondestructive inspection. Measurement 168, 108395.

ISO532-1, 2017. Acoustics–methods for calculating loudness–Part 1: Zwicker method. International Organization for Standardization Geneva, Switzerland.

Jiang, Y., Zhang, X., Taniguchi, T., 2019. Quantitative condition inspection and assessment of tunnel lining. Automation in Construction 102, 258 – 269.

Kurahashi, S., Mikami, K., Kitamura, T., Hasegawa, N., Okada, H., Kondo, S., Nishikino, M., Kawachi, T., Shimada, Y., 2018. Demonstration of 25-hz-inspection-speed laser remote sensing for internal concrete defects. Journal of Applied Remote Sensing 12, 015009.

Lei, M., Liu, L., Shi, C., Tan, Y., Lin, Y., Wang, W., 2021. A novel tunnel-lining crack recognition system based on digital image technology. Tunnelling and Underground Space Technology 108, 103724.

Loupos, K., Doulamis, A.D., Stentoumis, C., Protopapadakis, E., Makantasis, K., Doulamis, N.D., Amditis, A., Chrobocinski, P., Victores, J., Montero, R., et al., 2018. Autonomous robotic system for tunnel structural inspection and assessment. International Journal of Intelligent Robotics and Applications 2, 43–66.

Maierhofer, C., Arndt, R., Röllig, M., Rieck, C., Walther, A., Scheel, H., Hillemeier, B., 2006. Application of impulse-thermography for nondestructive assessment of concrete structures. Cement and Concrete Composites 28, 393 – 401.

Menendez, E., Victores, J.G., Montero, R., Martínez, S., Balaguer, C., 2018. Tunnel structural inspection and assessment using an autonomous robotic system. Automation in Construction 87, 117 – 126.

Meola, C., 2007. A new approach for estimation of defects detection with infrared thermography. Materials Letters 61, 747 – 750.

Mizutani, T., Yamaguchi, T., Kudo, T., Yamamoto, K., Ishida, T., Nagata, Y., Kawamura, H., Tokuno, T., Suzuki, K., Yamaguchi, Y., 2022. Quantitative evaluation of peeling and delamination on infrastructure surfaces by laser signal and image processing of 3d point cloud data. Automation in Construction 133, 104023.

Montero, R., Victores, J., Martínez, S., Jardón, A., Balaguer, C., 2015. Past, present and future of robotic tunnel inspection. Automation in Construction 59, 99 – 112.

Moreu, F., Ayorinde, E., Mason, J., Farrar, C., Mascarenas, D., 2018. Remote railroad bridge structural tap testing using aerial robots. International Journal of Intelligent Robotics and Applications 2, 67–80.

Mori, K., Spagnoli, A., Murakami, Y., Kondo, G., Torigoe, I., 2002. A new non-contacting non-destructive testing method for defect detection in concrete. NDT & E International 35, 399–406.

Nakamura, S., Yamashita, A., Inoue, F., Inoue, D., Takahashi, Y., Kamimura, N., Ueno, T., 2019. Inspection test of a tunnel with an inspection vehicle for tunnel lining concrete. Journal of Robotics and Mechatronics 31, 762–771.

Oh, T., Popovics, J.S., Ham, S., Shin, S.W., 2013. Improved interpretation of vibration responses from concrete delamination defects using air-coupled impact resonance tests. Journal of Engineering Mechanics 139, 315–324.

Omar, T., Nehdi, M.L., 2017. Remote sensing of concrete bridge decks using unmanned aerial vehicle infrared thermography. Automation in Construction 83, 360–371.

Protopapadakis, E., Voulodimos, A., Doulamis, A., Doulamis, N., Stathaki, T., 2019. Automatic crack detection for tunnel inspection using deep learning and heuristic image post-processing. Applied Intelligence 49, 2793–2806.

Ren, Y., Huang, J., Hong, Z., Lu, W., Yin, J., Zou, L., Shen, X., 2020. Image-based concrete crack detection in tunnels using deep fully convolutional networks. Construction and Building Materials 234, 117367.

Reynolds, D., Standlee, K., Angevine, E., 1977. Hand-arm vibration, part iii: Subjective response characteristics of individuals to hand-induced vibration. Journal of sound and vibration 51, 267–282.

Sakagami, T., Kubo, S., 2002. Development of a new non-destructive testing technique for quantitative evaluations of delamination defects in concrete structures based on phase delay measurement using lock-in thermography. Infrared Physics & Technology 43, 311 – 316.

Sugimoto, K., Sugimoto, T., Utagawa, N., Kuroda, C., 2019. Detection of resonance frequency of both the internal defects of concrete and the laser head of a laser doppler vibrometer by spatial spectral entropy for noncontact acoustic inspection. Japanese Journal of Applied Physics 58, SGGB15.

Tsuno, K., Kishida, K., 2020. Evaluation of spalling of concrete pieces from tunnel lining employing joint shear model. Tunnelling and Underground Space Technology 103, 103456.

Wakata, S., Hosoya, N., Hasegawa, N., Nisikino, M., 2022. Defect detection of concrete in infrastructure based on rayleigh wave propagation generated by laser-induced plasma shock waves. International Journal of Mechanical Sciences , 107039.

Wallace, C., 1972a. Radiation resistance of a baffled beam. The Journal of the Acoustical Society of America 51, 936–945.

Wallace, C., 1972b. Radiation resistance of a rectangular panel. The Journal of the Acoustical Society of America 51, 946–952.

Wang, H., Li, Y., Dang, L.M., Lee, S., Moon, H., 2021. Pixel-level tunnel crack segmentation using a weakly supervised annotation approach. Computers in Industry 133, 103545.

Xue, Y., Li, Y., 2018. A fast detection method via region-based fully convolutional neural networks for shield tunnel lining defects. Computer-Aided Civil and Infrastructure Engineering 33, 638–654.

Yasuda, N., 2022. Vibration characteristics of spalling defects in concrete lining. Tunnelling and Underground Space Technology 124, 104441.

Yasuda, N., Misaki, N., Shimada, Y., Kotyaev, O., 2021. Applicability of non-contact inspection using laser ablation-induced vibration in a reinforced concrete tunnel lining. Tunnelling and Underground Space Technology 113, 103977.

Yasuda, N., Misaki, N., Shimada, Y., Yamaoka, D., 2020. Detection and characteristics estimation of defects in concrete structures using laser ablation-induced vibration. Tunnelling and Underground Space Technology 103, 103460.

Zhou, M., Cheng, W., Huang, H., Chen, J., 2021. A novel approach to automated 3d spalling defects inspection in railway tunnel linings using laser intensity and depth information. Sensors 21, 5725.

Zhu, J., Popovics, J.S., 2007. Imaging concrete structures using air-coupled impact-echo. Journal of engineering mechanics 133, 628–640.

Table 1: Summary of concrete mix proportions.

Water cement ratio (%)	Fine aggregate ratio (%)	Water (kg/m^3)	Cement (kg/m^3)	Fine aggregate (kg/m^3)	Coarse aggregate (kg/m^3)	Admixture (kg/m^3)
68	46	190	270	800	990	2.7

Table 2: Material properties.

Parameters	Concrete	Air
Young's modulus (GPa)	29	
Poisson's ratio	0.20	
Density (kg/m^3)	2300	1.2
Sound speed (m/s)		340

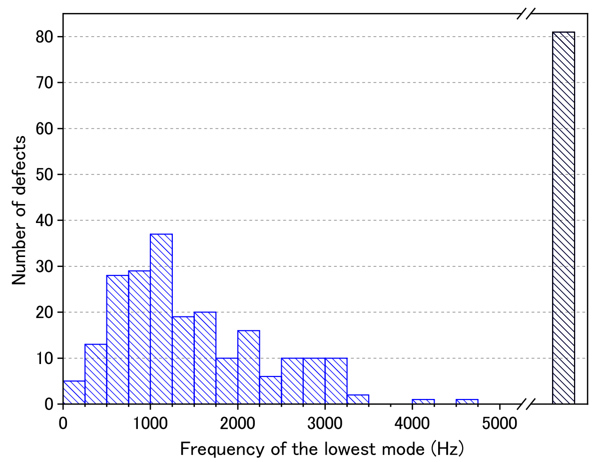

Figure 1: Distribution of lowest mode frequency in defect area rated as β in unreinforced concrete sections of tunnels.

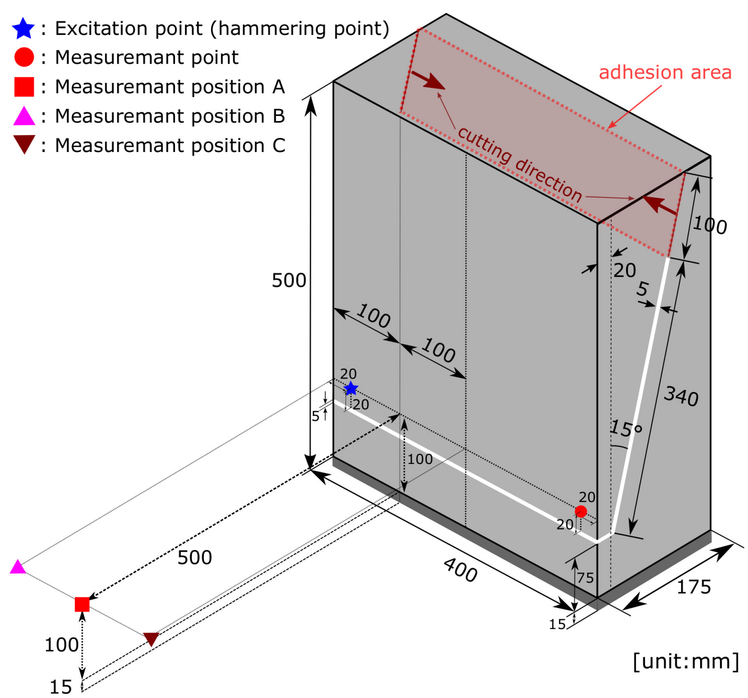

Figure 2: Dimensions of concrete specimen with vibration excitation and measurement points, and positions of sound pressure measurement.

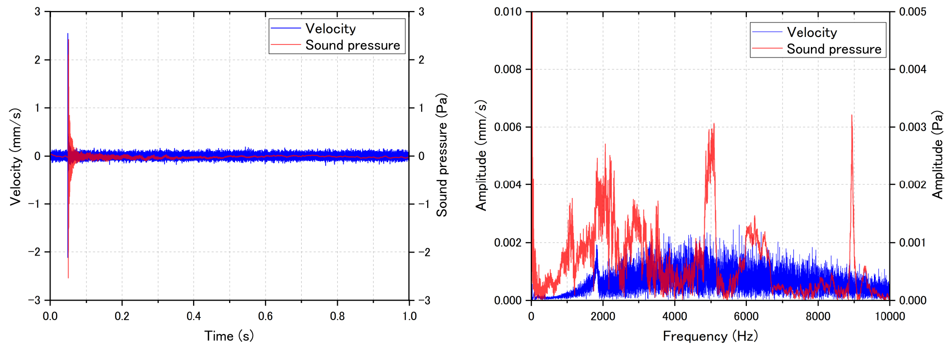

(a) (b)

Figure 3: Vibration and sound in good concrete: (a) time history waveforms; (b) Fourier spectra of waveforms.

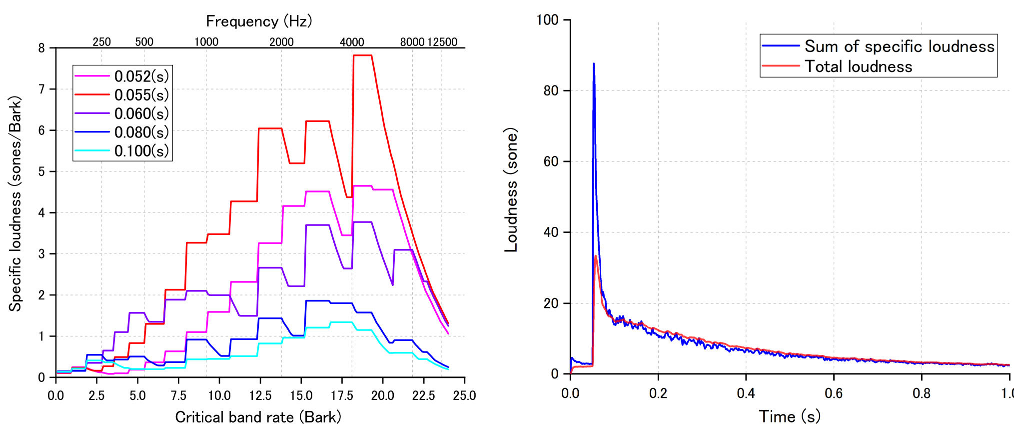

(a) (b)

Figure 4: Loudness of hammering sound in good concrete: (a) specific loudness; (b) total loudness.

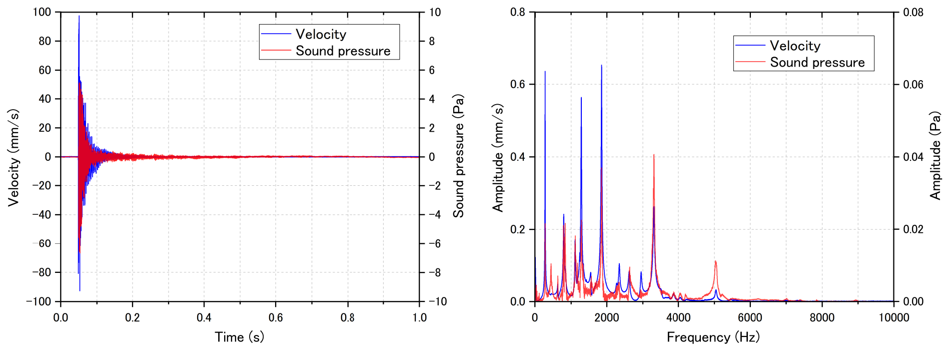

(a) (b)

Figure 5: Vibration and sound in specimen before cut: (a) time history waveforms; (b) Fourier spectra of waveforms. The sound was measured at position A.

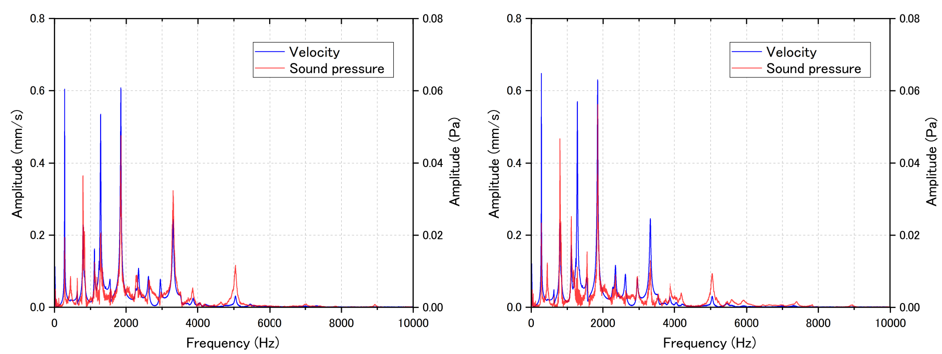

(a) (b)

Figure 6: Fourier spectra of vibration and sound in specimen before cut. The sounds were measured at (a) position B and (b) position C.

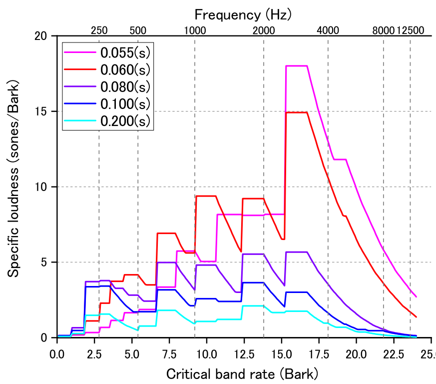

(a)

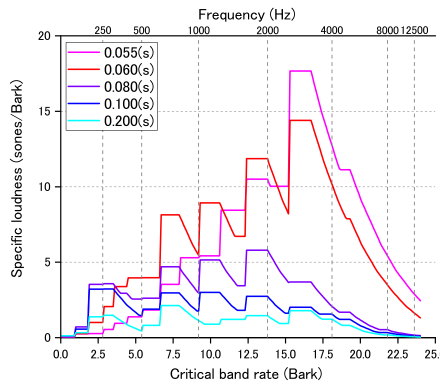

(b)

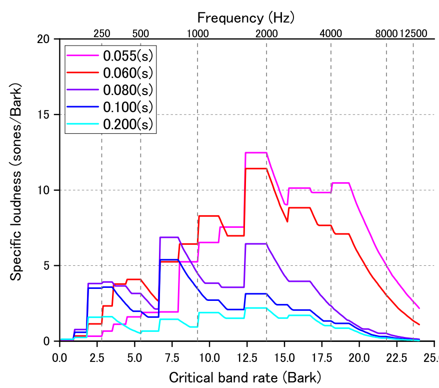

(c)

Figure 7: Specific loudness of hammering sound in specimen before cut. The sounds were measured at (a) position A, (b) position B, and (c) position C.

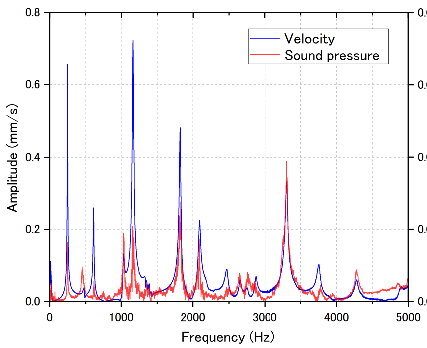

(a)

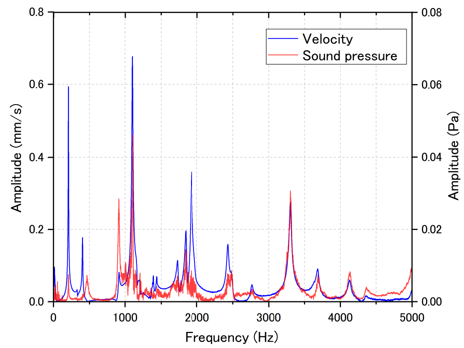

(b)

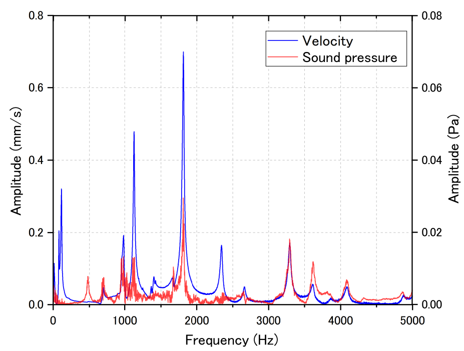

(c)

Figure 8: Change in Fourier spectra of vibration and sound with increase of cut length. The sound was measured at position A. The cut length was (a) 20 cm, (b) 30 cm, and (c) 38 cm.

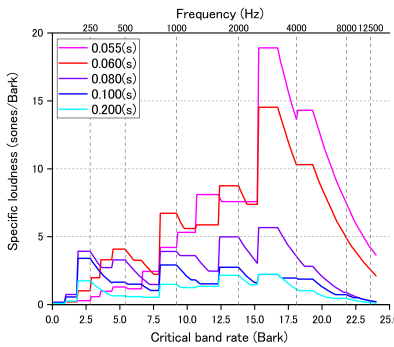

(a)

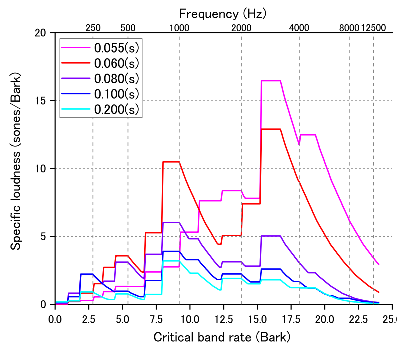

(b)

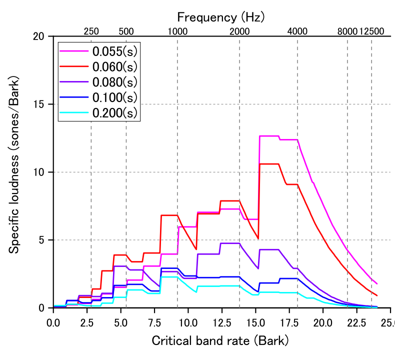

(c)

Figure 9: Change of specific loudness of sound with increase of cut length. The sound was measured at position A. The cut length was (a) 20 cm, (b) 30 cm, and (c) 38 cm.

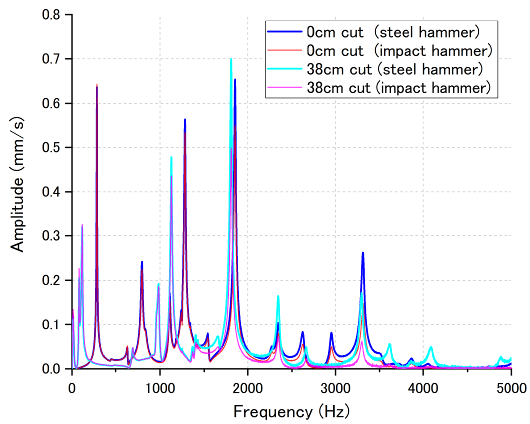

Figure 10: Comparison between Fourier spectra of vibration induced by steel hammer and Fourier spectra of vibration induced by impact hammer.

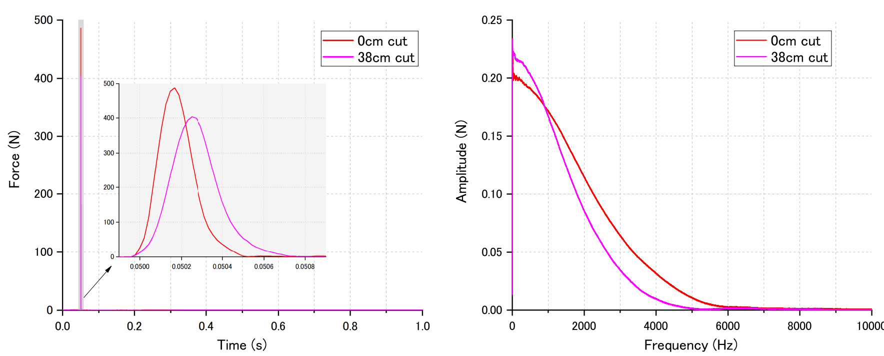

(a) (b)

Figure 11: Force signals induced by impact hammer: (a) time history waveforms; (b) Fourier spectra of these waveforms.

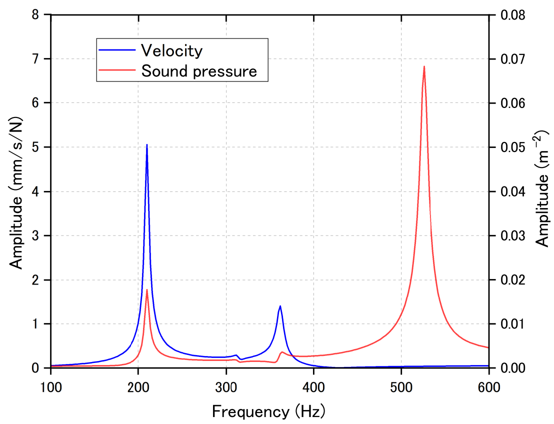

Figure 12: Frequency response functions obtained in specimen after cut of 30 cm, as obtained by numerical analysis. The sound was measured at position A.

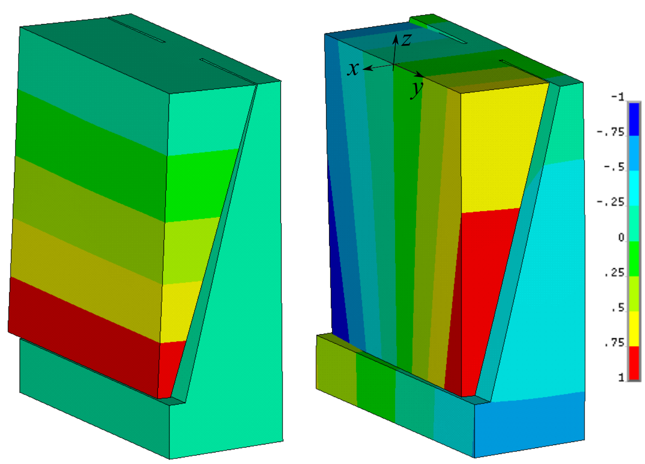

(a) (b)

Figure 13: Deformation in x-direction of low-order vibration modes in specimen after cut of 30 cm. The natural frequency was (a) 210 Hz and (b) 362 Hz.

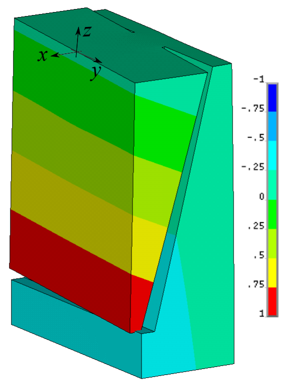

Figure 14: Deformation in z-direction of low-order vibration modes in specimen after cut of 30 cm. The natural frequency was 314 Hz.

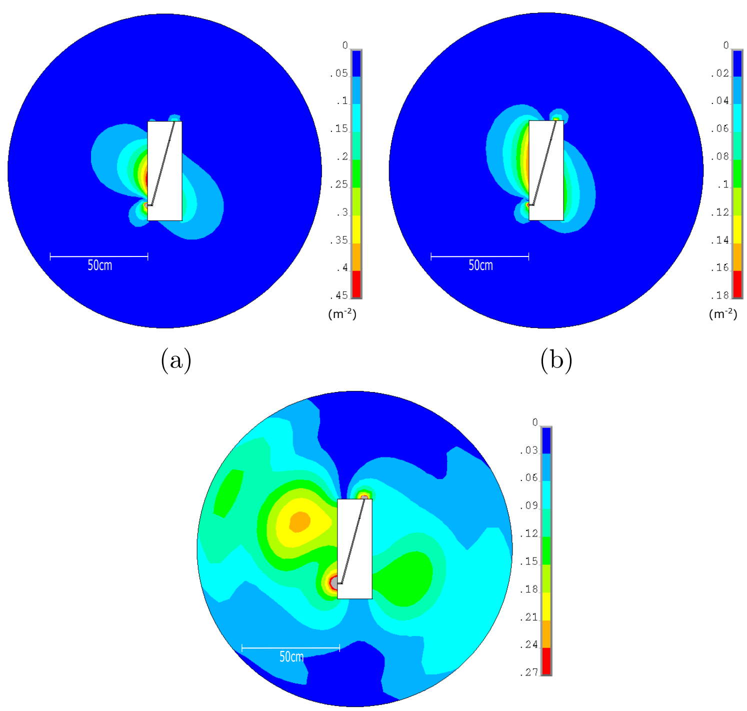

(a)

(b)

(c)

Figure 15: Spatial distribution of maximum sound pressure in specimen after cut of 30 cm on cross-section $y = -10$ (cm). The vibration frequency was (a) 210 Hz, (b) 362 Hz, and (c) 526 Hz.

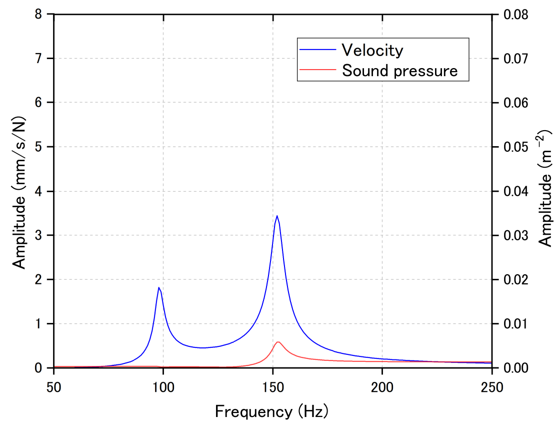

Figure 16: Frequency response functions in specimen after cut of 38 cm, as obtained by numerical analysis. The sound was measured at position A.

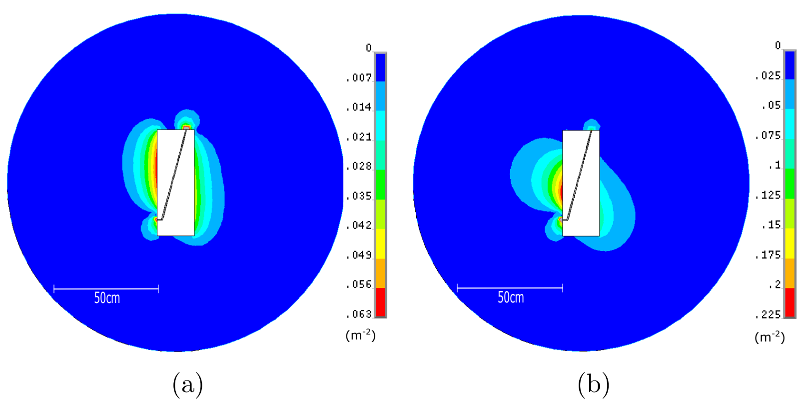

Figure 17: Spatial distribution of maximum sound pressure on cross-section $y = -10$ (cm) in specimen after cut of 38 cm. The vibration frequency was (a) 98 Hz and (b) 152 Hz.

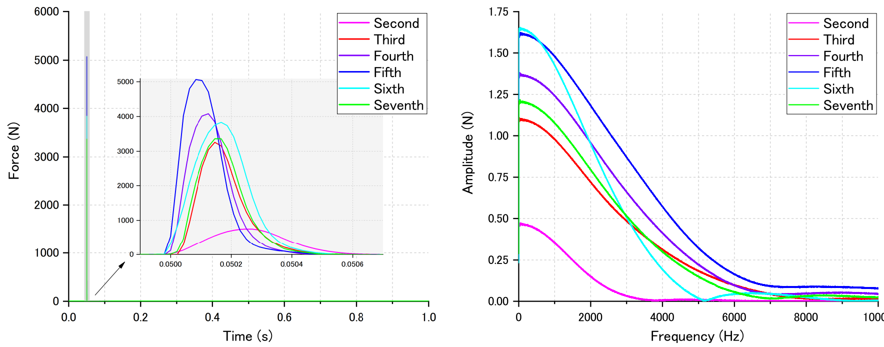

(a) (b)

Figure 18: Force signals induced by impact hammer. The cut length was 38 cm: (a) time history waveforms; (b) Fourier spectra of these waveforms.

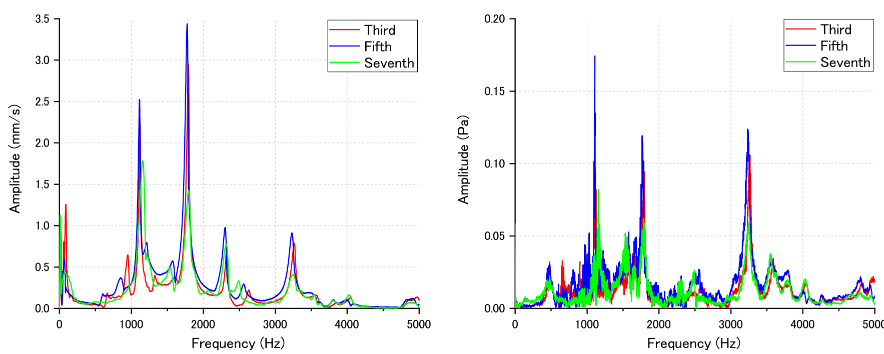

(a) (b)

Figure 19: Fourier spectra of (a) vibration and (b) sound induced by impact hammer. The cut length was 38 cm. The sound was measured at position A.

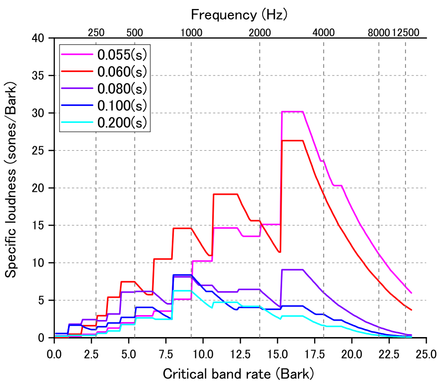

(a)

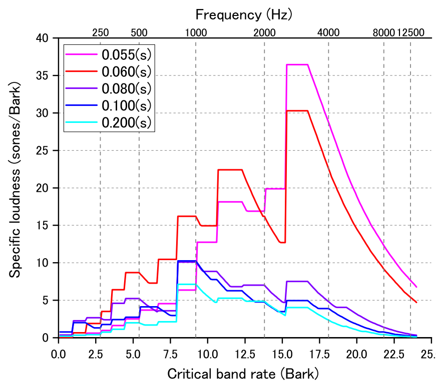

(b)

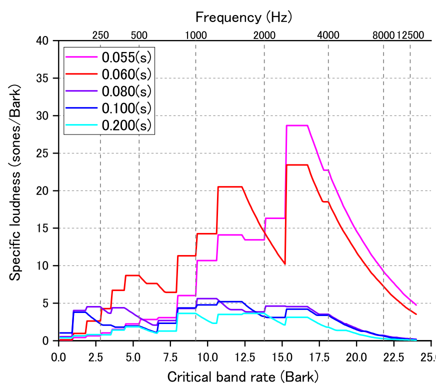

(c)

Figure 20: Specific loudness induced by impact hammer: (a) third impact; (b) fifth impact; (c) seventh impact. The cut length was 38 cm. The sounds were measured at position A.